

PAPER • OPEN ACCESS

Improved irradiation resistance of high entropy nanolaminates through interface engineering

To cite this article: Q Xu *et al* 2025 *Mater. Futures* 4 015301

View the [article online](#) for updates and enhancements.

You may also like

- [Pd-based Metallic Glasses as Promising Materials for Hydrogen Energy Applications](#)
Baran Sarac, A. Sezai Sarac and Jürgen Eckert
- [Normal stress effect on plastic yielding of notched metallic glass: a finite element simulation study](#)
Wen Zhong, Yanan Ren, Jing Hu *et al.*
- [Comparison of the Interfacial Reaction Kinetics and Plating Morphology of Lithium and Magnesium Anodes](#)
Yunsong Li, Zhe Liu, Yuxiao Lin *et al.*

Improved irradiation resistance of high entropy nanolaminates through interface engineering

Q Xu^{1,3}, J Eckert^{1,3} and D Şopu^{1,2,*} 

¹ Erich Schmid Institute of Materials Science, Austrian Academy of Sciences, Jahnstraße 12, A-8700 Leoben, Austria

² Institute of Materials Science, Technical University of Darmstadt, Otto-Berndt-Straße 3, D-64287 Darmstadt, Germany

³ Department of Materials Science, Chair of Materials Physics, Montanuniversität Leoben, Jahnstraße 12, A-8700 Leoben, Austria

E-mail: daniel.sopu@oaew.ac.at

Received 16 October 2024, revised 20 December 2024

Accepted for publication 6 January 2025

Published 29 January 2025



Abstract

Bi-phase interfacial engineering is an effective method for improving irradiation resistance, as interfaces play a critical role in defect generation and annihilation. In this work, molecular dynamics simulations are performed to investigate the evolution of the high entropy crystalline/amorphous laminates under ion irradiation. The effects of the crystalline/amorphous interface (ACI) on the distribution of point defects in the high entropy alloy (HEA) as well as on the microstructure evolution in metallic glass (MG) plates are investigated. During irradiation, fewer activated point defects were found in the HEA plate of the MG/HEA laminates compared to a free-standing HEA. In addition, the interface acts as a defect sink, accelerating the annihilation of interstitials at the interface. As a result, residual vacancies accumulate in the crystalline region following the first cascade, leading to a segregated distribution and an imbalance between the vacancies and interstitials in the HEA plate. Vacancy accumulation and clustering are responsible for the formation of stacking faults and complex dislocation networks in the HEA plate in the subsequent overlapping cascades. The interface also acts as a crystallization seed, accelerating the crystallization of the MG plate during irradiation process. However, the structural damage in the MG plate is mitigated by the redistribution of the free volume generated in the collision cascade zone, resulting in structural stability of the MG plate in the overlapping cascades.

Supplementary material for this article is available [online](#)

Keywords: high entropy alloy, metallic glass, irradiation, interface, molecular dynamics

* Author to whom any correspondence should be addressed.



Original Content from this work may be used under the terms of the [Creative Commons Attribution 4.0 licence](#). Any further distribution of this work must maintain attribution to the author(s) and the title of the work, journal citation and DOI.

1. Introduction

With the development of next generation nuclear reactors, the operating environment for nuclear structural materials is becoming more severe [1, 2]. One of the main challenges of fission reactors is the irradiation-induced structural damage, which leads to swelling, hardening, embrittlement and even failure of materials [3–5]. High entropy alloys (HEAs) have excellent mechanical properties and irradiation tolerance due to their single-phase solid solution with multi-principal element alloys [6, 7]. As demonstrated by theoretical and experimental studies, the high-level lattice distortion and compositional complexity can alter the energy dissipation process and promote the recovery of irradiation damage at the earlier stage of irradiation compared to conventional alloys [8, 9]. Most of the irradiation-induced vacancies are annihilated by the interstitials, i.e., the self-healing effects in the crystalline structures [10, 11].

Unlike crystalline alloys, there are no unit cells, grains, or grain boundaries in metallic glasses (MGs), so there is no possibility of well-defined crystallographic defects under irradiation [12]. However, it has been experimentally observed that the MGs have a high resistance to particle irradiation [13–15]. It has been shown that irradiation-induced transient vacancy-like defects are completely annihilated by free volume rearrangement after structural relaxation [16–18]. In addition, the irradiation-induced volume expansion (swelling) and embrittlement are suppressed in some amorphous alloys [19–21]. Unfortunately, the MGs are limited by the inherent shortcomings, such as structural relaxation and poor plasticity in extreme irradiation environments, which undermine their application to advanced nuclear materials [22, 23].

The introduction of a high-density interface, such as heterophases or grain boundaries, is a strategy for designing materials with high irradiation tolerance [24–26]. This method has been shown to be effective for some nuclear structural materials, such as oxide-dispersion-strengthened steels, nanolayered and nano-grained polycrystalline alloys [27–30]. The interfaces and grain boundaries, acting as defect sinks, can effectively promote defect annihilation and structural self-healing, thereby enhancing the structural stability and irradiation resistance [31, 32]. Meanwhile, it has been specifically reported that the irradiation-induced Fe/amorphous-FeZr interface can absorb defects and confine the movement of dislocation loops in crystalline layers [33]. By designing the Cu/Nb system, An *et al* found that nanolayered metallic composites with heterogeneous interfaces have better thermal stability, and the interactions between dislocations and interfaces can be effectively tuned by controlling the atomistic interface structure [34]. Furthermore, the interface-dominated materials can effectively eliminate the trade-offs that constrain conventional alloy design, while achieving superior irradiation tolerance, high strength and high thermal stability [35, 36].

Interfaces play a key role in determining the properties of interface-dominated materials. Most previous studies have focused on the irradiation resistance in the nanolaminates

with crystalline/crystalline interfaces and conventional alloys [37–39]. Rupert *et al* suggested that the amorphous phase introduced into the nanocrystalline structure can effectively increase the recombination rate of point defects and limit the growth of grain under irradiation [40, 41]. Also, the mobility of defects within interfaces depends on the interface properties and structure, and the sink efficiency of interfaces depends on the mobility of defects within the boundary plane [42]. Also, there are a number of studies that have revealed the mechanisms of excellent irradiation resistance for HEAs through molecular dynamics (MD) simulations, from the formation, evolution and distribution of point defects in the collision cascade [43, 44]. Furthermore, the MD method has been used to analyze the free volume and stress redistribution at the atomic scale in MG [45, 46]. Combining the irradiation tolerance of high-entropy crystalline and amorphous alloys with the interfacial structural response under irradiation offers a promising new strategy for designing materials with enhanced irradiation resistance. However, the application of such layered structures may raise some interesting and as yet unresolved questions. How does a laminar structure made of two HEAs behave under irradiation? How does the interface affect the defect distribution in MG/HEA nanolaminates? The answers to these critical questions will not only be beneficial for a thorough understanding of the irradiation mechanisms of MG/HEA nanolaminates, but will also provide a useful guideline for the design of irradiation tolerant materials. Studying the irradiation of MG/HEA nanolaminates using experimental techniques is challenging due to the difficulty in accurately analyzing the mechanisms at the atomic level.

In this work, a detailed study of the effects of the interface on the structural responses, defect dynamics and atomic mobility of MG/HEA nanolaminates under ion irradiation is carried out using the MD method. Firstly, the influence of the interfacial effects on the defect formation, evolution and distribution mechanisms in the HEA plate is investigated. Secondly, the effect of irradiation on structural relaxation and crystal nucleation and growth in the MG plate is evaluated by quantifying the fluctuations in free volume and excess entropy. Finally, the microstructural evolution during irradiation at the interface and the dislocation-interface interaction in MG/HEA nanolaminates are investigated in the overlapping cascades.

2. Simulation approach

In this work, the MD simulations of collision cascades were performed using the Large-scale Atomic/Molecular Massively Parallel Simulator (LAMMPS) [47]. Alloys with nominal compositions of $(\text{FeCoCrNi})_{100-x}\text{Al}_x$ were selected to generate the atomic models of the free-standing MG and HEA models and the MG/HEA nanolaminate. The atomic interactions were described using the Fe–Co–Cr–Ni–Al embedded atom method potential developed by Farkas and Caro [48]. In addition, the Ziegler–Biersack–Littmark repulsive potential was added to accurately describe the short-range interactions

during high-energy collision cascades. By adjusting the Al content in FeCoCrNiAl_x, both a face centered cubic (FCC) crystalline structure and an amorphous alloy can be formed during quenching process. First, 432 000 atoms were randomly distributed in a box of $21.6 \times 10.8 \times 21.6 \text{ nm}^3$ with periodic boundary conditions (PBCs) in all three directions and relaxed at 2000 K for 1 ns to ensure chemical homogeneity. Second, the melt was quenched from 2000 K to 300 K at 1 K ps^{-1} . During quenching, the FeCoCrNiAl_{1.7} composition stabilizes in an amorphous structure while FeCoCrNiAl_{0.5} shows a crystalline structure. The MG is stable and retains the glassy structure during annealing at elevated temperature close to the T_g (850 K). The MG/HEA laminate was constructed by superimposing the model of the MG plate and the HEA plate along the *y*-direction. For the MG plate, the model was relaxed in the *y*-direction (perpendicular to the interface of the MG/HEA laminate) while keeping the *x*- and *z*-directions fixed to maintain the same dimensions as the HEA plate during annealing. As a result, there are some small residual stresses in these two directions in the MG plate due to the effects of constrained thermal contraction. However, the residual stress components are less than 0.3 GPa. It has been shown that a slightly higher interfacial stress field contributes to the improved defect absorption capacity [37, 49]. Therefore, the interfacial stress field may also be an important factor in the irradiation response of the MG/HEA laminate [50]. Prior to the displacement cascade, all the models were relaxed to the equilibrium state at room temperature (300 K) lasting for 0.1 ns using an isobaric-isothermal (NPT) ensemble. The PBCs were applied in three dimensions along the *x* (1 0 0), *y* (0 1 0) and *z* (0 0 1) directions.

First, a Ni atom, selected as primary knock-on atom (PKA) with kinetic energy (E_{PKA}) of 10 keV was randomly positioned in the HEA plate of the MG/HEA laminate and launched at a certain distance away from the interface. In order to effectively study the effects of the interface on defect dynamics, the PKA was set up in the HEA plate to ensure that sufficient collisions occur in the HEA plate. The direction of the PKA is perpendicular to the interface (along the *y*-direction). To meet the requirement of the recoil energy to the number of atoms, the $60a_0 \times 60a_0 \times 60a_0$ unit cell (containing 864 000 atoms) is constructed for the E_{PKA} of 10 keV. To ensure the collision cascade passes through the interface, the distance between the PKA and the interface is set at 4 nm. During the irradiation process, the microcanonical (NVE) ensemble was applied to the displacement cascade atoms, while a N ose–Hoover thermostat was applied to the outermost layer of the simulation box, with a thickness of approximately three lattice units, to control the atomic velocities based on the target temperature (300 K). Use the Nose–Hoover thermostat only at the boundaries to absorb and dissipate excess heat and avoid the associated heating of the system. Keeping the core of the simulation box in an NVE ensemble ensures realistic dynamics during the collision process. A variable time step algorithm was implemented to speed up the simulations (generally from 0.0001 to 1 fs). The collision cascade simulation was completed in 100 ps. The further

relaxation process was applied to satisfy the requirement of fully stable atomic structures with a constant time step of 1 fs using the NPT ensemble for 0.1 ns after the collision cascade process. In order to better highlight the interfacial effects on the structural response and defect evolution during irradiation, overlapping cascades were applied to the nanolaminate sample. For each simulation, 10 collision cascades were performed for statistical purposes.

The open-source visualization software (OVITO) was used to analyze the simulation results [51, 52]. The irradiation-induced defects were detected using the Wigner–Seitz defect method, where the lattice sites with an empty atom are labelled as vacancies and the sites occupied by multiple atoms are labelled as interstitials. The dislocation lines and loops and stacking faults (SFs) in crystalline plate were identified using the dislocation extraction algorithm (DXA). The microstructure in crystalline plate was identified using common neighbor analysis [53, 54]. The stress or thermal-induced atomic rearrangement in the amorphous plate was revealed by the analysis of excess entropy and free volume. The free volume was calculated by Voronoi tessellation method implemented in OVITO [52]. The excess entropy was calculated based on the radial distribution function $g(r)$ [55], a modifier available in OVITO.

3. Collision cascade process

During the displacement cascade process, the high-energy PKA triggers collision and motion of some atoms in the nanolaminate, resulting in primary structural damage. The kinetic energy of the PKA is readily transferred to a number of colliding atoms, defined as knocked-on atoms, which is the origin of atomic motion and structural damage in the sample. Therefore, the evolution of knocked-on atoms is used to describe the collision cascade process. To visualize the zone where the collision cascades take place in the nanolaminate model, the spatial distributions of knocked-on atoms with kinetic energy higher than 0.4 eV during the displacement cascade process for the 1st cascade are shown in figure 1. The energy per atom of 0.4 eV is much higher than that caused by thermal vibrations, so there are no atoms with a kinetic energy greater than 0.4 eV in the nanolaminate model before irradiation.

In general, MD simulations have suggested that the collision cascade process has three main phases: an initial ballistic phase in which the atoms collide strongly, a subsequent thermal spike stage in which the high kinetic energy of the atoms dissipates into the surrounding matrix, and a thermal relaxation stage in which the structure cools and the crystal is usually left with a large number of defects [56]. Initially, the knocked-on atoms in the HEA plate spread rapidly, induced by high-energy PKA and approach to the interface position at 0.9 ps (figures 1(a) and (b)). The knocked-on atoms are then activated in the MG plate, and the collision cascade accordingly reaches a maximum value at 2.3 ps during the thermal

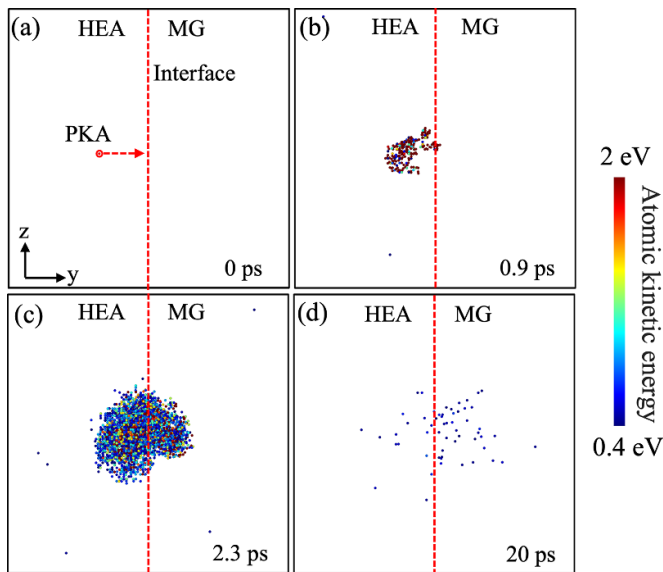


Figure 1. Spatial distribution of knocked-on atoms with a kinetic energy greater than 0.4 eV at the simulation time of 0 ps (a), 0.9 ps (b), 1.8 ps (c) and 20 ps (d) in the MG/HEA nanolaminate at the 1st cascade. The red arrow represents the direction of PKA.

spike stage as shown in figure 1(c). The region of the collision cascade with the maximum volume at the thermal spike is defined as the core of the cascade. After the thermal spike stage, the number of knocked-on atoms gradually decreases and almost disappears at 20 ps, indicating the end of the energy dissipation process (figure 1(d)). For the next overlapping cascades, the evolution of the collision cascade follows a similar trend. Further information on the specific distribution of the collision cascade core for the overlapping cascades is provided by the distribution of the knocked-on atoms at the thermal spike in the nanolaminate as shown in figure S1 in the supplementary material.

4. Defect evolution and distribution in the HEA plate

The point defects, including interstitials and vacancies are generated by the atomic displacement under the collision cascades of the energetic particles [57, 58]. The typical evolution of the number of defects with cascade time in the HEA plate of the laminate for the 1st and 10th cascade are shown in figure 2(a). The PKA excites some atoms which become interstitials, leaving corresponding vacancies, so that the number of interstitials and vacancies induced by ion irradiation is equal, called Frenkel pairs [59]. The evolution of the number of vacancies and interstitials in the HEA plate in the laminate follows a similar trend: a rapid increase at the start of the collision cascade, reaching a maximum value at the thermal spike stage. A fraction of the point defects then recombine and are annihilated during the thermal relaxation stage, while other defects survive.

To evaluate the effects of the ACI, the formation and evolution of defects in the HEA plate are compared with those in the free-standing HEA (the defect evolution in the free-standing HEA is shown in figure 2 in [60]). There are several obvious differences in the defect evolution in the HEA plate for the MG/HEA laminate. For the HEA plate in the 1st cascade, it has fewer defects at the thermal spike, almost a third of the free-standing HEA, but it has more surviving defects after thermal equilibrium (recombination) than the free-standing HEA [60]. The reduction in defects is due to energy diffusion into the interface and the amorphous phase. Part of the PKA energy is dissipated in the MG plate, as indicated by the knocked-on atoms activated in the MG plate across the interface (figure 1(b)). As the MG plate has no lattice structure, the Wigner–Seitz defect method cannot be used to analyze the defect structure. Therefore, the number of irradiation-induced point defects in the HEA plate is determined by the distribution of the collision cascade zone only in this plate. The number of vacancies becomes progressively higher than the number of interstitials after the collision cascade reaches the interface (0.9 ps) for the 1st cascade (see the solid lines in figure 2(a)). Even after structural relaxation (100 ps), there is still a difference between the number of residual vacancies and the number of interstitials.

For the 10th cascade the evolution of point defects follows the same trend as for the 1st cascade. It is worth noting that the difference between the number of residual vacancies and interstitials for the 10th cascade is much smaller than that for the 1st cascade (see the dashed lines in figure 2(a)). The fraction of residual vacancies and interstitials after structural relaxation for 10 overlapping cascades is shown in figure 2(b). The gap between the number of residual vacancies and interstitials decreases as the number of overlapping cascades increases, eventually reaching a dynamic equilibrium. The number of residual vacancies is almost equal to the number of interstitials after the 4th cascade. This means that as the number of overlapping cascades increases, the effect of the interface on the evolution of the point defects is weakened.

To further investigate the effect of the ACI on the propagation and accumulation of point defects, the spatial distribution of point defects in the HEA plate corresponding to the 1st cascade at cascade times of 1, 2.3, 10 and 100 ps is shown in figures 3(a)–(d). The vacancies and interstitials are represented by blue and red spheres respectively. The irradiation-induced vacancies and interstitials are randomly generated in the HEA plate without any effect of ACI before the collision cascade is spared to the interface (figure 3(a)). The number of vacancies is equal to the number of interstitials at this stage, which is consistent with the distribution in the free-standing HEA [60]. At the thermal spike, a rapid increase in the number of vacancies and interstitials is activated in the HEA plate (figure 3(b)). As more interstitials are attracted to the ACI due to the defective structure at the interface, this leads to an imbalance between the number of vacancies and interstitials (figure 2(a)). However, the distribution of vacancies and interstitials is uniform along the y-direction

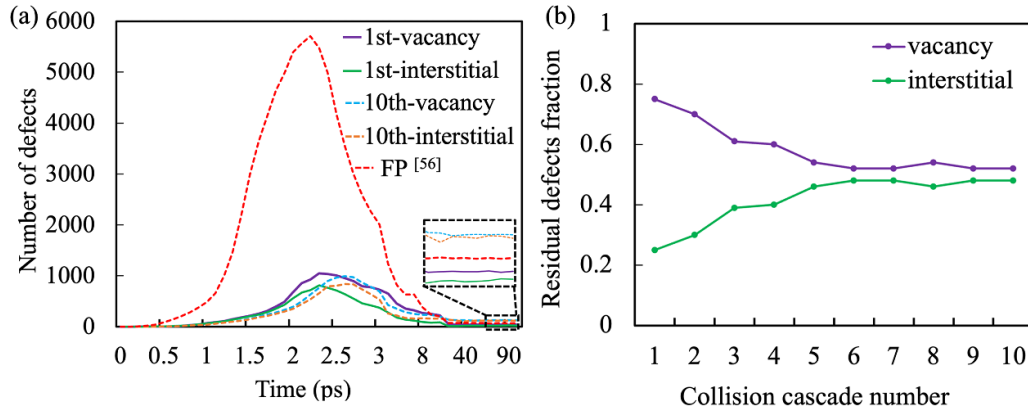


Figure 2. (a) Number of point defects versus simulation time for the 1st and 10th collision cascades in the HEA plate and the free-standing HEA. The inset dashed square displays the magnification for the number of defects after thermal relaxation. (b) Fraction of residual point defects after thermal relaxation in the HEA plate for 10 overlapping cascades.

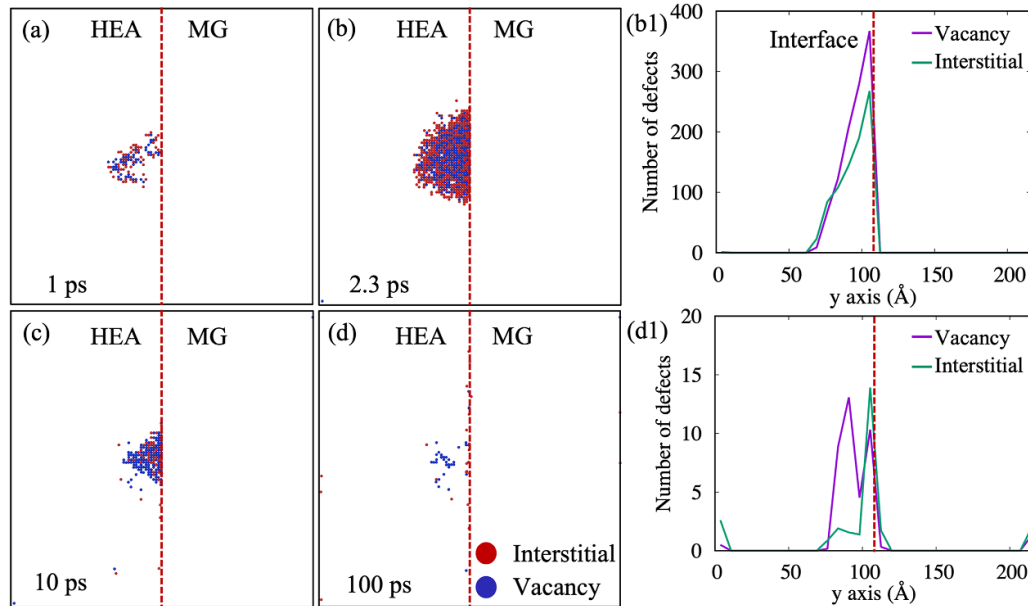


Figure 3. Spatial distribution of defects in the HEA plate at 1 ps (a), 2.3 ps (b), 10 ps (c) and 100 ps (d) in the 1st cascade. The corresponding distribution of defects at different distances from the interface along the y -direction at 2.3 ps (b1), 100 ps (d1).

as shown in figure 3(b1). Subsequently, most of the vacancies are recombined by the interstitials in the HEA plate during the thermal relaxation stage, resulting in a decrease in the number of defects. In addition, due to the higher mobility of the interstitials, more interstitials diffuse towards the interface and are preferentially adsorbed by the interface (figure 3(c)). In contrast to the interstitials, the vacancies have a significantly lower mobility and therefore the majority of the remaining vacancies are confined to the bulk of the HEA plate, away from the interface (figures 3(d) and (d1)). This shows a distinct distribution of vacancies and interstitials, with a vacancy-rich bulk and an interstitial-rich interface.

To analyze the interface effects on the distribution of point defects for the overlapping cascades, the spatial distribution of vacancies and interstitials for the 10th cascade at the cascade time of 1, 2.3, 10 and 100 ps is shown in figures 4(a)–(d). The vacancies and interstitials are uniformly distributed before the

knocked-on atoms approach the interfacial position, which is consistent with that in the 1st cascade (see figure 4(a)). With the collision cascade time, the point defects are rapidly generated and diffused in the HEA plate at the thermal spike (see figure 4(b)), and then most of the vacancies are annihilated by the interstitials during the thermal relaxation stage, resulting in the reduction of the point defects (see figure 4(c)). However, unlike the 1st cascade, the diffusion of interstitials to the interface is inhibited, resulting in more interstitials being trapped in the HEA plate. The distribution of vacancies and interstitials in the HEA plate after structural relaxation is more uniform than that in the 1st cascade (see figure 4(d)). The distribution of vacancies and interstitials across the interface is plotted at the thermal spike and thermal equilibrium stages in figures 4(b1) and (d1), respectively. There is no significant biased defect distribution in the HEA plate for the 10th cascade, compared to the 1st cascade (see figure 4(d1)). The

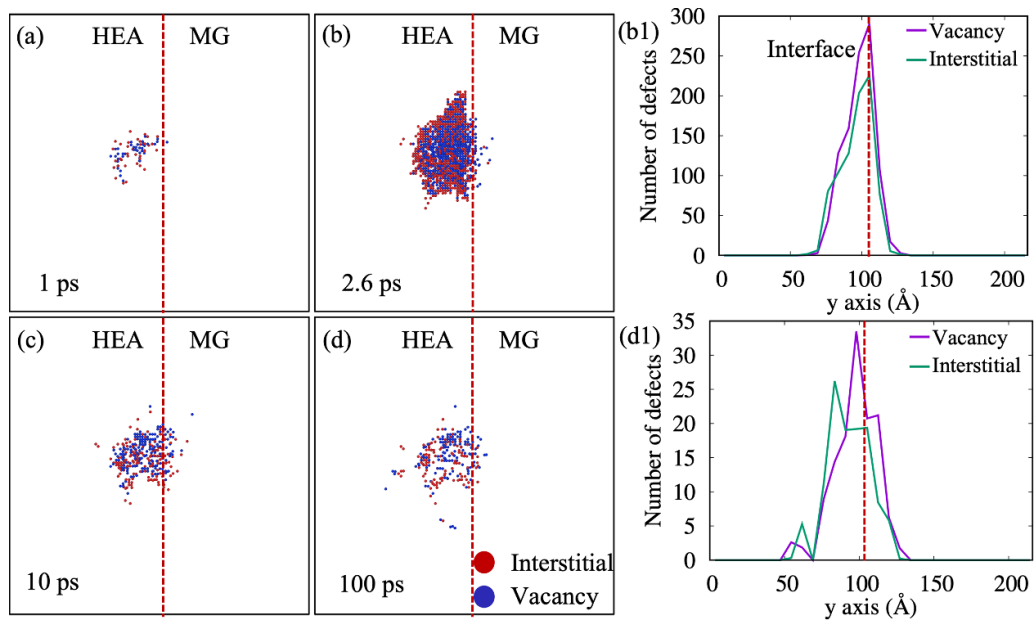


Figure 4. Spatial distribution of point defects in the HEA plate at 1 ps (a), 2.6 ps (b), 10 ps (c) and 100 ps (d) at the 10th cascade. The corresponding distribution of defects at different distances from the interface along the y-direction at 2.6 ps (b1), 100 ps (d1).

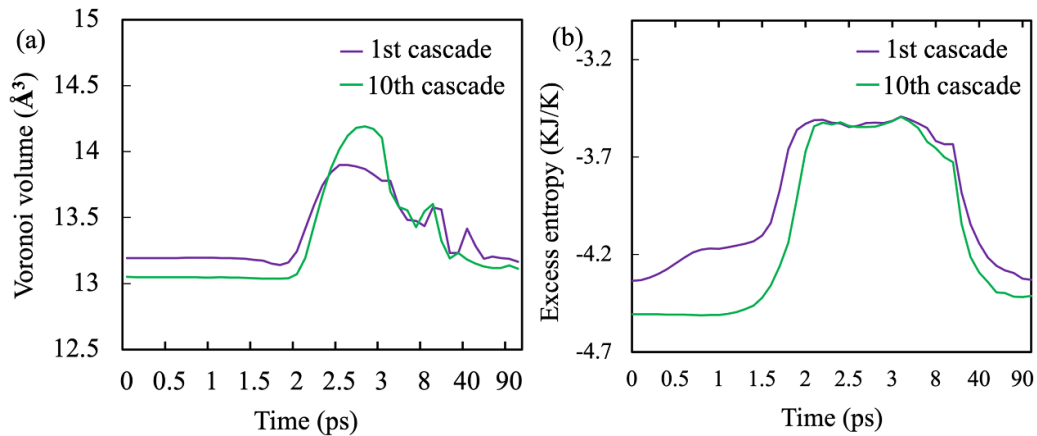


Figure 5. Evolution of (a) free volume and (b) local entropy of the collision cascade zone in the MG plate for the 1st and 10th cascades.

more uniform distribution of vacancies and interstitials in the bulk results in a smaller difference between the number of vacancies and interstitials after thermal relaxation for the following cascades. During the successive collision cascades, the microstructural changes in the HEA plate and in the ACI simultaneously influence the accumulation and distribution of point defect.

5. Structural responses in the MG plate

As mentioned above, the Wigner–Seitz defect method cannot analyze the structural defects in the amorphous phase. In order to evaluate the structural responses in the MG plate during irradiation, the evolution of the average atomic volume in the collision cascade cores for the 1st and 10th cascade is shown in figure 5(a). The free volume in the collision cascade core

increases rapidly as the collision cascade passes the interface and extends into the MG plate. The irradiation-induced atomic motion leads to the generation of the free volume in the MG plate. Subsequently, the free volume reaches a maximum value at the thermal spike, and then decreases after thermal relaxation, as can be seen in figure 5(a). The redistribution of the free volume is related to the structural relaxation of the MG plate. It is worth noting that, for the 1st cascade, the amount of the free volume after thermal equilibrium is slightly lower than that of the initial (non-irradiated) structure. This indicates that the ACI may affect the recombination of the free volume in the MG plate in the 1st cascade. For the 10th cascade it can be seen that the mean free volume at the beginning of the irradiation process is lower than the values of the 1st cascade, indicating a structural relaxation process during the overlapping cascades. Also, the maximum free volume at the thermal spike is significantly higher than for the 1st cascade. This is a direct result

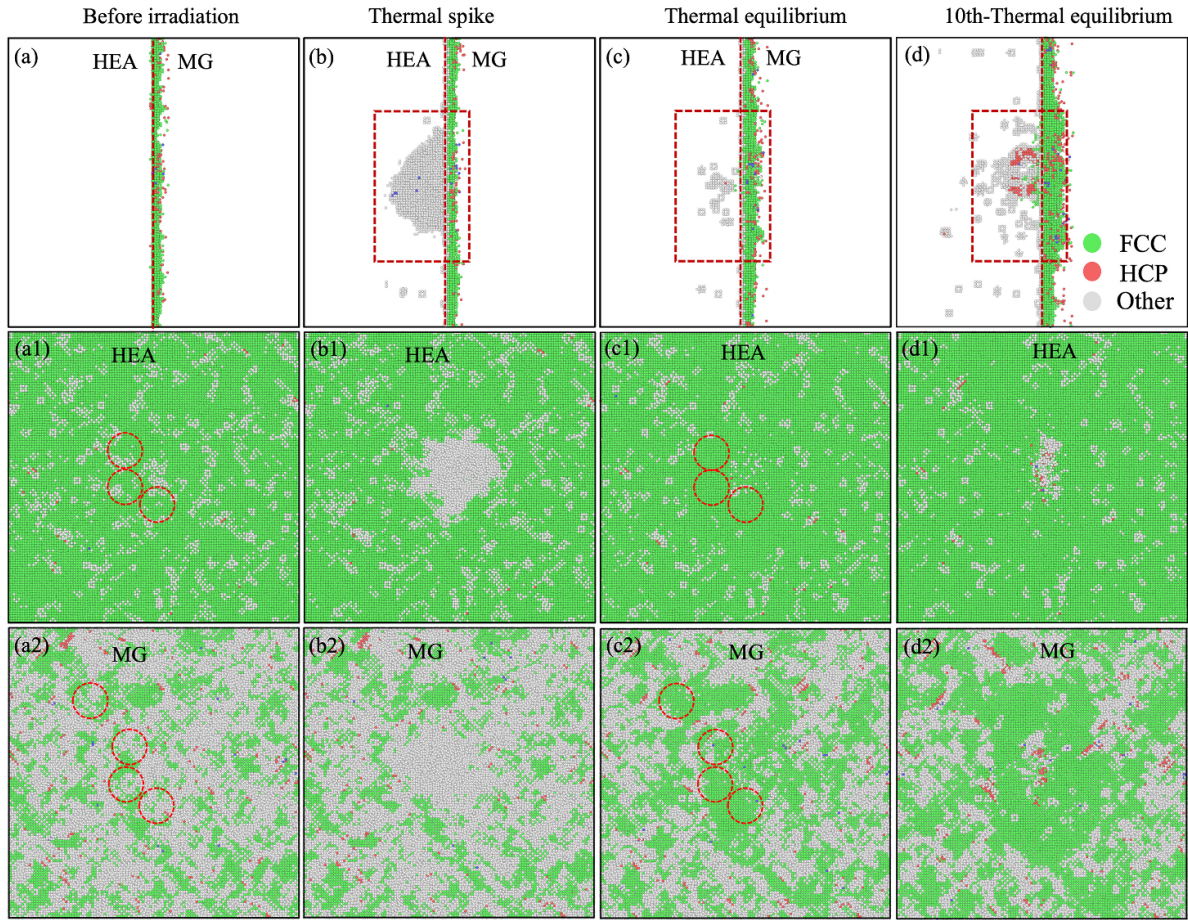


Figure 6. Microstructure configuration before irradiation (a), at the thermal spike (b), and after thermal relaxation (c) in the 1st cascade, and after thermal relaxation in the 10th cascade (d) in the laminate. All the atoms with FCC structure in HEA plate and all the atoms with amorphous phase in MG plate are deleted to clearly visualize the microstructure during irradiation. The interfacial microstructure in HEA and MG plates before irradiation (a1) and (a2), at the thermal spike (b1) and (b2), and after thermal relaxation (c1) and (c2) in the 1st cascade, and after thermal relaxation in the 10th cascade (d1) and (d2).

of the higher energy from PKA that is introduced into the MG plate, leading to a greater expansion of the free volume at the core of the collision cascade. In addition, the free volume after thermal equilibrium for the 10th cascade is lower than that for the 1st cascade, indicating a continuous decrease of the free volume in the collision cascade core during relaxation with the overlapping cascades.

The movement of the knocked-on atoms and the expansion of the free volume induce the structural disorder in the MG plate. The excess entropy evolution is further used to quantify the structural disorder in the collision cascade core during the irradiation process for the 1st and 10th cascades, as shown in figure 5(b) [61, 62]. The excess entropy follows the same trend as the evolution of the free volume but shows a wider distribution. Also, during the thermal spike, the excess entropy for both the 1st and 10th cascades reaches comparable levels. This suggests that, while the energy diffused into the MG plate causes varying degrees of configurational changes, the excess entropy remains unaffected at this stage. The free volume reflects the configurational aspects of the structure, while the excess entropy consists of both configurational information and vibrational contributions [63, 64], leading to the difference

in the evolution of atomic volume and excess entropy. As a result, the excess entropy is also sensitive to the initial shock wave generated during the irradiation process. After thermal relaxation, the excess entropy for the 10th cascade is significantly lower and smoother compared to the 1st cascade, indicating that structural relaxation in the MG plate becomes progressively enhanced with overlapping cascades. In summary, the heat injected into the collision cascade zone during irradiation facilitates free volume recombination and promotes interfacial crystallization in the nanolaminates.

6. Microstructural evolution in nanolaminate

To further reveal the ACI effects on the structural responses under irradiation, the microstructural evolution in HEA and MG plates, as well as at the interface for the nanolaminate, is analyzed. The microstructural evolution of the nanolaminate before irradiation, at the thermal spike and after thermal relaxation for the 1st cascade is shown in figures 6(a)–(c). The atoms with FCC and amorphous phase are represented by green and gray spheres respectively. All the atoms with

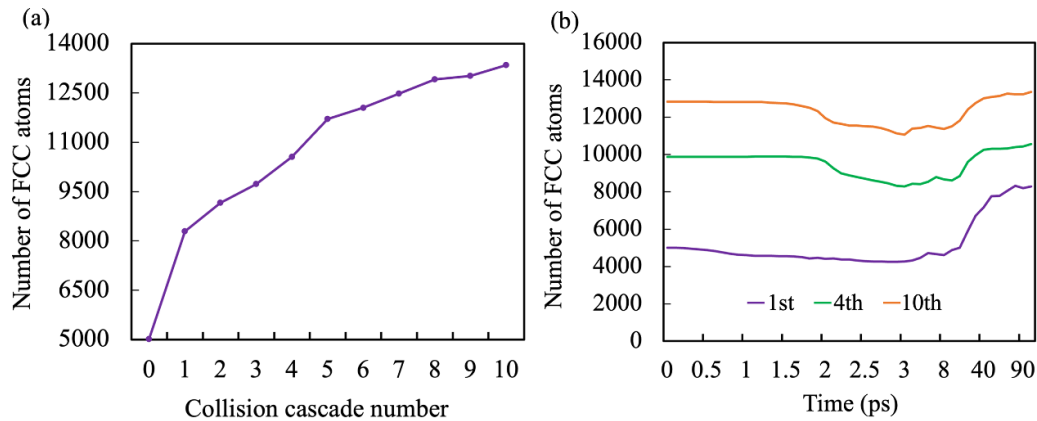


Figure 7. (a) Number of atoms with FCC structure in MG plate at the interface for 10 overlapping cascades. (b) Evolution of the number of atoms with FCC structure in MG plate at the interface at the 1st, 4th, and 10th cascades.

FCC structure in HEA plate and all the atoms with amorphous phase in MG plate are deleted to clearly visualize the microstructure during the irradiation process. Before irradiation, the stress mismatch between the crystalline and amorphous plates leads to the crystallization and formation of defects in the MG plate at the interface (figure 6(a)) [36]. During irradiation, the high energy introduced by PKA spreads into the laminate, inducing localized melting in the collision cascade zone, as shown in figure 6(b). In addition, free volume expansion and weakened structural stability occur at the collision cascade core in the MG plate (figure 5). The variation of the temperature per atom with time in the cascade core of the nanolaminate is shown in figure S2 in the supplementary material. At the initial irradiation stage, the temperature of the collision cascade core is much higher than the melting point of the HEA and MG plates, and then rapidly decreases to room temperature during the thermal relaxation stage. This leads to local atomic rearrangement and recrystallization in the HEA plate (figure 6(c)) and relaxation of the free volume in the MG plate. Most importantly, the structural healing in the HEA plate triggers the atomic rearrangement in the MG plate at the interface, leading to the crystallization of the MG plate at the interface, as shown by the red dashed square in figure 6(c). Furthermore, after the 10th cascade, there is a significant increase in the crystallization at the interface in the MG plate, as shown by the red dashed square in figure 6(d). It should be noted that irradiation of bulk MGs at room temperature leads to structural relaxation and a decrease in free volume content, but never triggers crystallization [18, 20], as shown in figure S3 in the supplementary material. This suggests that the partial crystallization observed at the interface in the MG plate during irradiation is driven by interfacial effects. This partial crystallization in the MG plate can also explain the decrease in free volume within the overlapping cascades (figure 5).

Details of the evolution of the interfacial structure in the HEA and MG plates before irradiation, at the thermal spike and thermal relaxation stages for the 1st cascade are shown in figures 6(a1), (b1), (c1) and (a2), (b2), (c2), respectively. For the interfacial structure in the HEA plate, there are some disordered regions resulting from the stress mismatch between

HEA and MG plates before irradiation, as shown by the red dashed circles in figure 6(a1). The irradiation induced atomic displacement leads to the phase transformation from FCC to amorphous phase in the collision cascade zone (gray atoms in figures 6(b1) and (b2)). Subsequently, during the thermal relaxation, the atomic rearrangement in the collision cascade zone leads to the more ordered structure at the ACI in the HEA plate compared to the initial structure, as shown by the red dashed circles in figure 6(c1). In addition, the more disordered structure is generated in the collision cascade zone in the HEA plate after the 10th overlapping cascade (see figures 6(d1)). With further irradiation, the MG plate continues to crystallize at the position of the collision cascade zone (see figures 6(a2) and (c2) for comparison). The chemical composition in the crystalline phase in the MG plate is further calculated after 10 overlapping collision cascades. The Al content in the crystalline region of the MG plate decreases from the initial content of 30 at.% to 20 at.%, while the contents of the other four elements are very close to 20 at.%. This means that the composition of the crystalline phase in the MG plate has an equi-atomic ratio after the irradiation-induced atomic diffusion and rearrangement. Therefore, the crystallization in MG plate is accompanied by the compositional transition which together with the presence of a crystallization seed (HEA plate), triggers crystal nucleation and growth in the MG plate. After the 10th overlapping cascade, the local crystallization at the interface is significantly larger compared to the 1st cascade, as shown in figures 6(c2) and (d2).

The evolution of the number of atoms with FCC structure in the MG plate with the overlapping cascades is shown in figure 7(a). The crystallization of the MG plate at the interface shows a continuous increase, although it gradually slows down with successive overlapping cascades. The local melting induced by the irradiation process increases the atomic mobility, which drives the atomic rearrangements at the interface, leading to the further crystallization of the MG plate at the interface. To further elucidate the slowdown in crystallization within the overlapping cascades, figure 7(b) shows the evolution of the number of atoms with an FCC structure in the collision cascade zone in the MG plate at the 1st, 4th, and

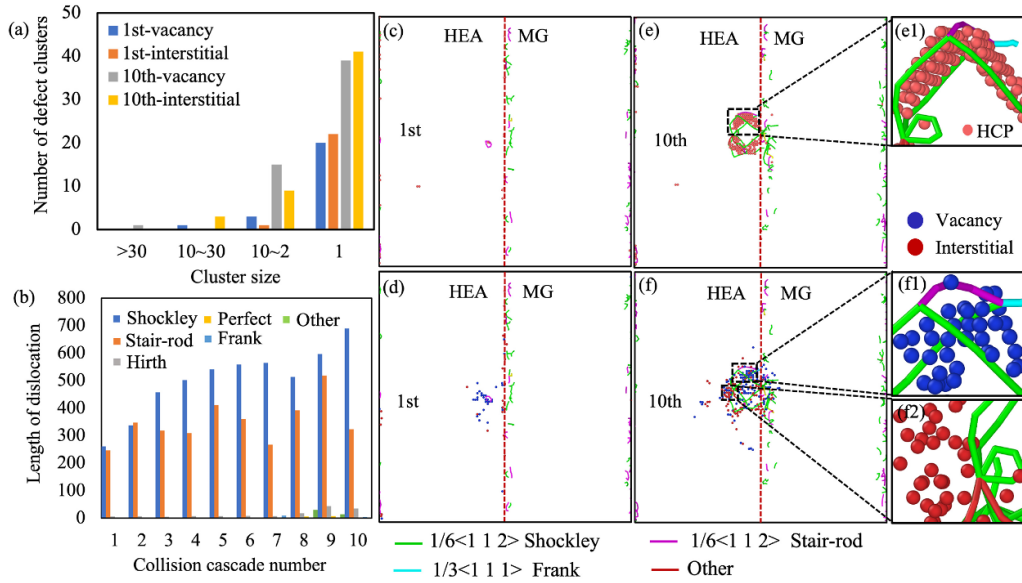


Figure 8. (a) Number of vacancies and interstitials in clusters in HEA plate for the 1st and 10th cascades. (b) The length of dislocations after 10 overlapping cascades in the nanolaminate. Snapshots of microstructure and dislocation distribution at (c) the 1st cascade and (e) the 10th cascade after structural relaxation. Snapshots of defects and dislocation distribution at (d) the 1st cascade and (f) the 10th cascade after structural relaxation. (e1) The detailed view of the dislocation distribution with stacking faults for the corresponding magnifications of the dashed square in (e). The detailed view of the accumulated (f1) vacancies and (f2) interstitials with the dislocation loops, respectively.

10th cascades. In the 1st cascade, there is a greater increase in the number of atoms with FCC structure during the thermal relaxation stage, indicating the greater influence of the interface on the crystallization in the MG plate. As the number of overlapping cascades increases, the effect of the interface on crystallization is reduced. Initially, there is a significant reduction in the FCC structure during the thermal spike stage due to the local melting caused by the irradiation process followed by an increase in the number of FCC atoms during the subsequent relaxation stage. A plausible explanation for this behavior is the compositional transition at the interface caused by irradiation-induced atomic diffusion and rearrangement. As the crystalline phase in the MG plate approaches an equiatomic composition (20 at.% for each element), the chemical equilibrium at the interface reduces the driving force for further diffusion and crystallization. In addition, the compositional mismatch between the crystalline region and the surrounding amorphous matrix creates a barrier that makes further diffusion energetically less favorable.

It is well known that the movement and interaction between dislocation loops during the defect evolution can lead to different defect distributions and microstructures [65, 66]. To understand the relationship between the distribution of point defects and the dislocation network during irradiation, the defect clustering and dislocation structures in the HEA plate for the 1st and 10th cascade are analyzed in figure 8(a). For the 1st cascade, large vacancy clusters with more than 10 vacancies are formed in the HEA plate away from the interface. On the other hand, the interstitials trapped in the interface region appear almost as a single interstitial. Compared to the 1st cascade, more complex defect clusters are formed for the 10th cascade as the number of overlapping cascades increases. A greater number of vacancies and interstitial clusters accumulate in the

HEA plate after thermal relaxation, including medium (the cluster with 2–10 defects) and large (the cluster with more than 10 defects) interstitial clusters as well as single defects. Thus, the more disordered structure occurs in the collision cascade zone after the 10th cascade compared to the 1st cascade (see figures 6(c1) and (d1)). To clarify the interface effects on defect interaction, the details of the dislocation and defect distributions after thermal relaxation for the 1st and 10th cascades are shown in figures 8(b)–(f). The length of different kind of dislocations after 10 overlapping cascades in the nanolaminate is displayed in the figure 8(b). After collision cascades, the dislocation lines exhibit the Shockley and Stair-rod. The length of the Shockley dislocation increases with the increasing number of collision cascades. The more complex dislocations, e.g. Perfect and Frank dislocations generate with the further interaction between defects and dislocations. For the 1st cascade, there is almost no formation of SFs and dislocation loops due to the high recombination rate in the HEA plate after the structural relaxation (figures 8(c) and (d)). However, some interstitials diffuse into the interface where they are trapped, leading to the accumulation of vacancies in the HEA bulk. The corresponding vacancies accumulate and forms large-size vacancy clusters that generate SFs and dislocations [60]. Then, the further interaction between defects and dislocation lines within the overlapping cascades trigger the more residual defect clusters and SF accumulation in the HEA plate, as shown in figures 8(e) and (f). This interfacial effects accelerate the formation of more complex dislocation structures and SFs in the HEA plate compared to that in the free-standing HEA (The comparison of dislocation structures between the free-standing HEA and the nanolaminate after the overlapping cascades is displayed in figure S4 in supplementary material). The formation of some order SFs is related to the formation of a

complex dislocation network in the HEA plate, which inhibits the mobility of vacancies and interstitials (figure 8(e)). A representative SF is shown in figure 8(e1). The SFs and the complex dislocation network around them lead to more interstitials being trapped in the bulk, which explains the more uniform distribution of point defects in subsequent collision cascades. Meanwhile, the suppressed mobility of point defects inhibits the recombination of vacancies and interstitials, generating a greater number of defect clusters in the HEA plate, as shown in figure 8(f). The interstitial and vacancy clusters accumulate between these dislocation loops as shown in figures 8(f1) and (f2) respectively. The propagation of dislocation loops further hinders the recombination and annihilation of vacancies and interstitials. Thus, the limited mobility and recombination of interstitials as the vacancies in the bulk of the HEA plate leads to the smaller difference between the number of residual vacancies and interstitials after structural relaxation in the next collision cascades. Details of the evolution of defects and dislocations after thermal relaxation for these 10 overlapping cascades are shown in figure S5 in supplementary material.

7. Conclusions

In this work, the high entropy crystalline/amorphous laminates under ion irradiation have been studied by means of MD simulations. The atomic scale effects of ACI on the distribution of point defects and microstructural evolution in HEA and MG plates have been revealed. The main findings are summarized as follows:

1. Compared to the free-standing HEA, the high energy PKA activates a lower number of point defects in the HEA plate because part of the PKA energy is absorbed in the MG plate of the laminate. In addition, the ACI acts as a sink, trapping most of the interstitials. The corresponding vacancies accumulate in the bulk of the HEA plate, leading to a significant separation of vacancies and interstitials into vacancy-rich bulk and interstitial-rich interface after the 1st cascade.
2. During irradiation, the MG plate undergoes a structural relaxation process resulting in a reduction in free volume. The HEA plate also acts as a seed for crystallization, triggering crystal nucleation and growth in the MG plate at the position of the collision cascade core. Crystallization in the MG plate is accompanied by a compositional transition, with the Al content decreasing from an initial 30 at.% to 20 at.%.
3. As the number of overlapping cascades increases, more interstitials are trapped in the ACI, while vacancies conglomerate and form vacancy clusters in the bulk of the HEA plate, leading to the formation of SFs and dislocation loops. These SFs and the complex dislocation network act as a barrier, reducing the mobility of the point defects and inhibiting further migration of interstitials to the interface. A weaker interfacial effect results in a more uniform distribution and almost equal number of vacancies and interstitials after thermal relaxation in the HEA plate for the

further overlapping cascades. In the overlapping cascades, the effect of the interface on crystallization in the MG plate is also reduced due to the compositional transition at the interface, which reduces the driving force for crystallization. With further irradiation, structural damage in the MG plate is mitigated by free volume redistribution, resulting in structural stability of the MG plate.

These results provide an atomistic picture of the interfacial effects in high entropy amorphous/crystalline nanolaminates under ion irradiation, which may provide strategies for designing materials with high irradiation tolerance.

8. Future perspectives

The results of this study clearly demonstrate that the enhanced irradiation resistance of high entropy nanolaminates provides a robust basis for advancing materials design for extreme environments. The synergistic combination of high entropy crystalline and amorphous phases highlights the potential for developing advanced nuclear materials with tailored properties. However, a significant gap remains in the understanding of the role of interfaces in defect formation and interaction in HEAs, particularly in comparison with other interface types. The high entropy crystalline and amorphous nanolaminates open up several avenues for future research:

The potential of bi-phase interfaces as defect sinks, focusing on interfacial stress fields, chemical gradients and phase boundaries to improve defect recombination efficiency, needs to be systematically investigated. The exploration of alternative material combinations and the incorporation of elements with tailored diffusion and bonding properties may further improve irradiation tolerance. Beyond irradiation resistance, understanding the behavior of MG/HEA nanolaminates under mechanical stress, thermal cycling and corrosive environments is critical. Long-term performance studies, particularly under high temperature and neutron flux conditions, can assess the viability of these materials for nuclear and aerospace applications. Therefore, future work should address the challenges of scaling up the synthesis of MG/HEA nanolaminates while maintaining structural integrity and interfacial properties. Advances in additive manufacturing techniques, such as directed energy deposition or selective laser melting, may enable the production of larger, more complex components with nanolaminate structures.

The unique combination of irradiation resistance and mechanical stability in MG/HEA nanolaminates positions them as candidates for new applications. Beyond nuclear reactors, these materials could be explored for advanced microelectronics, wear resistant coatings and components in extreme chemical environments. High-resolution characterization techniques, including *in situ* transmission electron microscopy, atom probe tomography and synchrotron-based x-ray diffraction, are essential to gain detailed insights into structural stability, defect dynamics and interfacial mechanisms. Furthermore, it is essential to reveal the atomic-level behavior at MG/HEA interfaces under irradiation to enable

precise fine-tuning of nanolaminate structures to achieve optimal performance. The integration of computational simulations with experimental observations can accelerate the optimization of high-entropy nanolaminates. Advanced MD models that predict the interplay between irradiation-induced cascades and interfacial phenomena can guide experimental designs, reducing cost and development time. By addressing these challenges, future research will pave the way for the design of next-generation materials with unparalleled performance in demanding environments, significantly expanding the applications of high-entropy nanolaminates.

Acknowledgments

The authors acknowledge financial support by the China Scholarship Council (CSC, No. 202008430162). The authors are grateful for the computing time granted by the Lichtenberg high performance computer of Technische Universität Darmstadt. Additional computation time was made available on the JFRS-1 supercomputer system at Computational Simulation Centre of International Fusion Energy Research Centre (IFERC-CSC) in Rokkasho Fusion Institute of QST (Aomori, Japan).

ORCID iD

D Şopu  <https://orcid.org/0000-0001-5531-462X>

References

- [1] Abram T and Ion S 2008 Generation-IV nuclear power: a review of the state of the science *Energy Policy* **36** 4323–30
- [2] Locatelli G, Mancini M and Todeschini N 2013 Generation IV nuclear reactors: current status and future prospects *Energy Policy* **61** 1503–20
- [3] Zhang X *et al* 2018 Radiation damage in nanostructured materials *Prog. Mater. Sci.* **96** 217–321
- [4] Azevedo C 2011 A review on neutron-irradiation-induced hardening of metallic components *Eng. Fail. Anal.* **18** 1921–42
- [5] Odette G, Alinger M and Wirth B 2008 Recent developments in irradiation-resistant steels *Annu. Rev. Mater. Res.* **38** 471–503
- [6] Xia S Q, Wang Z, Yang T F and Zhang Y 2015 Irradiation behavior in high entropy alloys *J. Iron Steel Res. Int.* **22** 879–84
- [7] Cheng Z, Sun J, Gao X, Wang Y, Cui J, Wang T and Chang H 2023 Irradiation effects in high-entropy alloys and their applications *J. Alloys Compd.* **930** 166768
- [8] Zong M, Chen F, Tang X, Ge G, Li C and Liu Y 2022 Molecular dynamics simulation of radiation defect evolution mechanism of NiFe-graphene nanocomposite *Appl. Surf. Sci.* **584** 152503
- [9] Xia S Q, Yang X, Yang T F, Liu S and Zhang Y 2015 Irradiation resistance in Al_xCoCrFeNi high entropy alloys *JOM* **67** 2340–4
- [10] Sadeghilaridjani M, Ayyagari A, Muskeri S, Hasannaemi V, Salloom R, Chen W Y and Mukherjee S 2020 Ion irradiation response and mechanical behavior of reduced activity high entropy alloy *J. Nucl. Mater.* **529** 151955
- [11] Kumar N K, Li C, Leonard K, Bei H and Zinkle S 2016 Microstructural stability and mechanical behavior of FeNiMnCr high entropy alloy under ion irradiation *Acta Mater.* **113** 230–44
- [12] Wang W, Dong C and Shek C 2004 Bulk metallic glasses *Mater. Sci. Eng. R* **44** 45–89
- [13] Wang Y, Zhang K, Feng Y, Li Y, Tang W, Zhang Y, Wei B and Hu Z 2019 Excellent irradiation tolerance and mechanical behaviors in high-entropy metallic glasses *J. Nucl. Mater.* **527** 151785
- [14] Wang B, Mei X, Zhang H, Hou W, Wang Y, Wang Z and Dong C 2014 Resistance to He²⁺ induced irradiation damage in metallic glass Zr₆₄Cu_{17.8}Ni_{10.7}Al_{7.5} *J. Nucl. Mater.* **444** 342–8
- [15] Bian X *et al* 2016 Manipulation of free volumes in a metallic glass through Xe-ion irradiation *Acta Mater.* **106** 66–77
- [16] Yang L *et al* 2017 Structural responses of metallic glasses under neutron irradiation *Sci. Rep.* **7** 16739
- [17] Dong Y F, Li M F, Malomo B and Yang L 2021 Microstructural evolution in ZrCu metallic glass under neutron irradiation *Comput. Mater. Sci.* **188** 110183
- [18] Mayr S G 2005 Impact of ion irradiation on the thermal, structural and mechanical properties of metallic glasses *Phys. Rev. B* **71** 144109
- [19] Avchaciov K A, Ritter Y, Djurabekova F, Nordlund K and Albe K 2013 Controlled softening of Cu₆₄Zr₃₆ metallic glass by ion irradiation *Appl. Phys. Lett.* **102** 181910
- [20] Magagnosc D, Kumar G, Schroers J, Felfel P, Cairney J and Gianola D 2014 Effect of ion irradiation on tensile ductility, strength and fictive temperature in metallic glass nanowires *Acta Mater.* **74** 165–82
- [21] Huang Y, Fan H, Zhou X, Xue P, Ning Z, Daisenberger D, Sun J and Shen J 2015 Structure and mechanical property modification of a Ti-based metallic glass by ion irradiation *Scr. Mater.* **103** 41–44
- [22] Trexler M M and Thadhani N N 2010 Mechanical properties of bulk metallic glasses *Prog. Mater. Sci.* **55** 759–839
- [23] Sadeghilaridjani M, Ayyagari A, Muskeri S, Hasannaemi V, Jiang J and Mukherjee S 2019 Small-scale mechanical behavior of ion-irradiated bulk metallic glass *JOM* **72** 123–9
- [24] Han W, Demkowicz M J, Mara N A, Fu E, Sinha S, Rollett A D, Wang Y, Carpenter J S, Beyerlein I J and Misra A 2013 Design of radiation tolerant materials via interface engineering *Adv. Mater.* **25** 6975–9
- [25] Jiao L, Chen A, Myers M, General M, Shao L, Zhang X and Wang H 2013 Enhanced ion irradiation tolerance properties in TiN/MgO nanolayer films *J. Nucl. Mater.* **434** 217–22
- [26] Huang L, Chen Z, Liu W, Huang P, Meng X, Xu K, Wang F and Lu T 2019 Enhanced irradiation resistance of amorphous alloys by introducing amorphous/amorphous interfaces *Intermetallics* **107** 39–46
- [27] Hirata A, Fujita T, Wen Y R, Schneibel J H, Liu C T and Chen M W 2011 Atomic structure of nanoclusters in oxide-dispersion-strengthened steels *Nat. Mater.* **10** 922–6
- [28] Odette G R 2014 Recent progress in developing and qualifying nanostructured ferritic alloys for advanced fission and fusion applications *JOM* **66** 2427–41
- [29] Zhang Y, Ishimaru M, Varga T, Oda T, Hardiman C, Xue H, Katoh Y, Shannon S and Weber W J 2012 Nanoscale engineering of radiation tolerant silicon carbide *Phys. Chem. Chem. Phys.* **14** 13429
- [30] Sun C *et al* 2015 Superior radiation-resistant nanoengineered austenitic 304L stainless steel for applications in extreme radiation environments *Sci. Rep.* **5** 7801
- [31] Prakash R, Amirthapandian S, Phase D, Deshpande S, Kesavamoorthy R and Nair K 2006 Study of ion beam induced mixing in nano-layered Si/C multilayer structures *Nucl. Instrum. Methods Phys. Res. B* **244** 283–8

- [32] Cui B, Kacher J, McMurtrey M, Was G and Robertson I 2014 Influence of irradiation damage on slip transfer across grain boundaries *Acta Mater.* **65** 150–60
- [33] Wang P W, Jing H Y, Li M F, Malomo B and Yang L 2022 Effective self-healing behavior of nanocrystalline-amorphous laminated alloy under irradiation *J. Appl. Phys.* **132** 225105
- [34] An Q, Yang W, Liu B and Zheng S 2020 Interface effects on the properties of Cu–Nb nanolayered composites *J. Mater. Res.* **35** 2684–700
- [35] Ma Y, Chen H, Zhang M-X, Addad A, Kong Y, Lezaack M B, Gan W, Chen Z and Ji G 2023 Break through the strength-ductility trade-off dilemma in aluminum matrix composites via precipitation-assisted interface tailoring *Acta Mater.* **242** 118470
- [36] Xu Q, Şopu D, Yuan X, Kiener D and Eckert J 2022 Interface-related deformation phenomena in metallic glass/high entropy nanolaminates *Acta Mater.* **237** 118191
- [37] Wang M, Beyerlein I J, Zhang J and Han W-Z 2018 Defect-interface interactions in irradiated Cu/Ag nanocomposites *Acta Mater.* **160** 211–23
- [38] Jin Y, Huang H, Zhong Y, Yuan X, Li H, Lou D, Xie K, Liu Z, Cai B and Peng Q 2022 Role of interface on irradiation damage of Cu–diamond composites using classical molecular dynamics simulations *Ceram. Int.* **48** 16813–24
- [39] Lin G, Jiang L and Ji P 2023 The effect of enhanced heat transfer across metal–nonmetal interfaces subject to femtosecond laser irradiation *Phys. Chem. Chem. Phys.* **25** 19853–67
- [40] Ludy J E and Rupert T J 2016 Amorphous intergranular films act as ultra-efficient point defect sinks during collision cascades *Scr. Mater.* **110** 37–40
- [41] Schuler J D, Grigorian C M, Barr C M, Boyce B L, Hattar K and Rupert T J 2020 Amorphous intergranular films mitigate radiation damage in nanocrystalline Cu–Zr *Acta Mater.* **186** 341–54
- [42] Beyerlein I, Demkowicz M, Misra A and Uberuaga B 2015 Defect-interface interactions *Prog. Mater. Sci.* **74** 125–210
- [43] Wang R, Chen Z, Shu Y, Lin Y, Liu Z, Deng H, Hu W and Yang T 2023 Molecular dynamics simulation of effects of Al on the evolution of displacement cascades in AlCoCrFeNi high entropy alloys *J. Nucl. Mater.* **577** 154342
- [44] Deluigi O, Pasianot R, Valencia F, Caro A, Farkas D and Bringa E 2021 Simulations of primary damage in a high entropy alloy: probing enhanced radiation resistance *Acta Mater.* **213** 116951
- [45] Avchaciov K, Ritter Y, Djurabekova F, Nordlund K and Albe K 2014 Effect of ion irradiation on structural properties of Cu₆₄Zr₃₆ metallic glass *Nucl. Instrum. Methods Phys. Res. B* **341** 22–26
- [46] Fu E, Carter J, Martin M, Xie G, Zhang X, Wang Y, Littleton R and Shao L 2009 Electron irradiation-induced structural transformation in metallic glasses *Scr. Mater.* **61** 40–43
- [47] Plimpton S 1995 Fast parallel algorithms for short-range molecular dynamics *J. Comput. Phys.* **117** 1–19
- [48] Farkas D and Caro A 2020 Model interatomic potentials for Fe–Ni–Cr–Co–Al high-entropy alloys *J. Mater. Res.* **35** 3031–40
- [49] Uglov V, Zlotski S, Abadias G and Veremei I 2022 Influence of helium ion irradiation on the stress evolution in nc-ZrN/a-ZrCu multilayered films *8th Int. Congress on Energy Fluxes and Radiation Effects, EFRE-2022*
- [50] Yang K et al 2021 Enhanced defect annihilation capability of the graphene/copper interface: an in situ study *Scr. Mater.* **203** 114001
- [51] Stukowski A 2009 Visualization and analysis of atomistic simulation data with OVITO—the open visualization tool *Modelling Simul. Mater. Sci. Eng.* **18** 015012
- [52] Stukowski A 2012 Structure identification methods for atomistic simulations of crystalline materials *Modelling Simul. Mater. Sci. Eng.* **20** 045021
- [53] Devincze B and Kubin L 1997 Mesoscopic simulations of dislocations and plasticity *Mater. Sci. Eng. A* **234–236** 8–14
- [54] Faken D and Jónsson H 1994 Systematic analysis of local atomic structure combined with 3D computer graphics *Comput. Mater. Sci.* **2** 279–86
- [55] Piaggi P M and Parrinello M 2017 Entropy based fingerprint for local crystalline order *J. Chem. Phys.* **147** 114112
- [56] Bolse W 1994 Ion-beam induced atomic transport through bi-layer interfaces of low- and medium-Z metals and their nitrides *Mater. Sci. Eng. R* **12** vii–viii, 53–121
- [57] Chiang H, Park S, Mayer M, Schmid K, Balden M, Boesenberg U, Jungwirth R, Falkenberg G, Zweifel T and Petry W 2015 Swift heavy ion irradiation induced interactions in the UMo/X/Al trilayer system (X = Ti, Zr, Nb and Mo): RBS and μ -XRD studies *J. Alloys Compd.* **626** 381–90
- [58] Toloczko M, Garner F, Voyevodin V, Bryk V, Borodin O, Mel'nychenko V and Kalchenko A 2014 Ion-induced swelling of ODS ferritic alloy MA957 tubing to 500 dpa *J. Nucl. Mater.* **453** 323–33
- [59] Lin Y, Yang T, Lang L, Shan C, Deng H, Hu W and Gao F 2020 Enhanced radiation tolerance of the Ni-Co-Cr-Fe high-entropy alloy as revealed from primary damage *Acta Mater.* **196** 133–43
- [60] Xu Q, Yuan X, Eckert J and Şopu D 2024 Crack-healing mechanisms in high-entropy alloys under ion irradiation *Acta Mater.* **263** 119488
- [61] Şopu D, Yuan X, Moitzi F, Spieckermann F, Bian X and Eckert J 2021 From elastic excitations to macroscopic plasticity in metallic glasses *Appl. Mater. Today* **22** 100958
- [62] Şopu D, Moitzi F, Mousseau N and Eckert J 2020 An atomic-level perspective of shear band formation and interaction in monolithic metallic glasses *Appl. Mater. Today* **21** 100828
- [63] Smith H L et al 2017 Separating the configurational and vibrational entropy contributions in metallic glasses *Nat. Phys.* **13** 900–5
- [64] Şopu D, Yuan X, Spieckermann F and Eckert J 2024 Coupling structural, chemical composition and stress fluctuations with relaxation dynamics in metallic glasses *Acta Mater.* **275** 120033
- [65] Robach J S, Robertson I M, Wirth B D and Arsenlis A 2003 In-situ transmission electron microscopy observations and molecular dynamics simulations of dislocation-defect interactions in ion-irradiated copper *Phil. Mag.* **83** 955–67
- [66] Ghoniem N, Tong S, Huang J, Singh B and Wen M 2002 Mechanisms of dislocation-defect interactions in irradiated metals investigated by computer simulations *J. Nucl. Mater.* **307–311** 843–51